Poznań University of Technology

Doctoral Thesis

Method for direct noise analysis of transonic axial compressor blade

Author:
MSc. Eng. Jędrzej Mosiężny

Supervisor:
Prof. DSc. Eng. Michał Ciałkowski

A thesis submitted in fulfilment of the requirements for the degree of Doctor of Philosophy. Engineer.

in the

Faculty of Work Machines and Transportation
Chair of Thermal Engineering

August 21, 2018

Declaration of Authorship

I, MSc. Eng. Jędrzej Mosiężny, declare that this thesis titled, 'Method for direct noise analysis of transonic axial compressor blade' and the work presented in it are my own. I confirm that:

- This work was done wholly or mainly while in candidature for a research degree at this University.
- Where any part of this thesis has previously been submitted for a degree or any other qualification at this University or any other institution, this has been clearly stated.
- Where I have consulted the published work of others, this is always clearly attributed.
- Where I have quoted from the work of others, the source is always given. With the exception of such quotations, this thesis is entirely my own work.
- I have acknowledged all main sources of help.
- Where the thesis is based on work done by myself jointly with others, I have made clear exactly what was done by others and what I have contributed myself.

Signed: ____________________

Date: ____________________

Abstract

This thesis proposes a method of assessing flow generated noise in transonic flows by direct formulation.

First a steady state Reynolds Averaged Navier-Stokes analysis of NASA R67 transonic axial compressor is performed as a validation study of the mesh and numerical setup. The result of the steady state analysis is then used as an initialization for transient DDES analysis performed on high quality, 11 million cells hexagonal mesh. The transient analysis covers 0.05s of physical flow time, which corresponds to about 800 revolutions of the rotor. Both steady state and transient simulations are performed on PL-Grid HPC infrastructure.

Transient results are analyzed with an in-house build program. The program uses information about static pressure, transient particle velocity and vorticity from each timestep. This data is then postprocessed into sound pressure levels, sound frequency and effective sound power level.

Information on generation of sound phenomena occurring in the blade passage are gathered from direct formulation and may be used as a validation case for FW-H or other computational aeroacoustic analogies dealing with flows in transonic regimes in rotating machinery.

Acknowledgements

In this place I would like to thank the Chair of Thermal Engineering of Poznań University of Technology, with special recognition to MSc. Eng. Bartosz Ziegler and PhD Eng. Przemysław Grzymisławski for thorough scientific and personal support during this project.

A big recognition goes to the owners and maintainers of the PLGRID - Polish HPC infrastructure, especially team in HPC Cyfronet center in AGH University of Science and Technology in Kraków. Being able to use the state of the art HPC clusters for analyses made this project possible.

Contents

List of Figures

List of Tables

Abbreviations

CAA	**C**omputional **A**ero **A**coustics
CFD	**C**omputional **F**luid **D**ynamics
DDES	**D**elayed **D**etached **E**ddy **S**imulation
DES	**D**etached **E**ddy **S**imulation
HPC	**H**ight **P**ower **C**omputing
LES	**L**arge **E**ddy **S**imulation
N-S	**N**avier **S**tokes
SRS	**S**cale **R**resolving **S**imulation

Symbols

a	distance	m
P	power	W (Js^{-1})
ω	angular frequency	$rads^{-1}$

To my wife. For limitless patience. . .

Chapter 1

Introduction

1.1 Main Section 1

Lorem ipsum dolor sit amet, consectetur adipiscing elit. Aliquam ultricies lacinia euismod. Nam tempus risus in dolor rhoncus in interdum enim tincidunt. Donec vel nunc neque. In condimentum ullamcorper quam non consequat. Fusce sagittis tempor feugiat. Fusce magna erat, molestie eu convallis ut, tempus sed arcu. Quisque molestie, ante a tincidunt ullamcorper, sapien enim dignissim lacus, in semper nibh erat lobortis purus. Integer dapibus ligula ac risus convallis pellentesque.

Lorem ipsum dolor sit amet, consectetur adipiscing elit. Aliquam ultricies lacinia euismod. Nam tempus risus in dolor rhoncus in interdum enim tincidunt. Donec vel nunc neque. In condimentum ullamcorper quam non consequat. Fusce sagittis tempor feugiat. Fusce magna erat, molestie eu convallis ut, tempus sed arcu. Quisque molestie, ante a tincidunt ullamcorper, sapien enim dignissim lacus, in semper nibh erat lobortis purus. Integer dapibus ligula ac risus convallis pellentesque.

1.1.1 Subsection 1

Nunc posuere quam at lectus tristique eu ultrices augue venenatis. Vestibulum ante ipsum primis in faucibus orci luctus et ultrices posuere cubilia Curae; Aliquam erat volutpat. Vivamus sodales tortor eget quam adipiscing in vulputate ante ullamcorper. Sed eros ante, lacinia et sollicitudin et, aliquam sit amet augue. In hac habitasse platea dictumst.

1.1.2 Subsection 2

Morbi rutrum odio eget arcu adipiscing sodales. Aenean et purus a est pulvinar pellentesque. Cras in elit neque, quis varius elit. Phasellus fringilla, nibh eu tempus venenatis, dolor elit posuere quam, quis adipiscing urna leo nec orci. Sed nec nulla auctor odio aliquet consequat. Ut nec nulla in ante ullamcorper aliquam at sed dolor. Phasellus fermentum magna in augue gravida cursus. Cras sed pretium lorem. Pellentesque eget ornare odio. Proin accumsan, massa viverra cursus pharetra, ipsum nisi lobortis velit, a malesuada dolor lorem eu neque.

1.2 Main Section 2

Sed ullamcorper quam eu nisl interdum at interdum enim egestas. Aliquam placerat justo sed lectus lobortis ut porta nisl porttitor. Vestibulum mi dolor, lacinia molestie gravida at, tempus vitae ligula. Donec eget quam sapien, in viverra eros. Donec pellentesque justo a massa fringilla non vestibulum metus vestibulum. Vestibulum in orci quis felis tempor lacinia. Vivamus ornare ultrices facilisis. Ut hendrerit volutpat vulputate. Morbi condimentum venenatis augue, id porta ipsum vulputate in. Curabitur luctus tempus justo. Vestibulum risus lectus, adipiscing nec condimentum quis, condimentum nec nisl. Aliquam dictum sagittis velit sed iaculis. Morbi tristique augue sit amet nulla pulvinar id facilisis ligula mollis. Nam elit libero, tincidunt ut aliquam at, molestie in quam. Aenean rhoncus vehicula hendrerit.

Chapter 2

Current research on Computational Aeroacoustics

2.1 Classification of CAA methods

Computational aeroacoustics is a branch of aeroacoustics that aims to analyze the generation of noise by turbulent flows through numerical methods. A following classification of available methods is currently in use.

1. Hybrid Approach.
   - (a) Integral Method
     - i. Lighthill's Analogy
     - ii. Kirchoff Integral
     - iii. FW-H
   - (b) Linearized Euler Equations
   - (c) Pseudo Spectral
   - (d) EIF
   - (e) APE
2. Direct approach.

The direct approach is the core of this thesis and will be described in detail in chapter 3. A brief introduction to Lightill's analogy with Curle's modification is provided below. Ffowcs Williams Hawkings analogy as an extension to the theory is also provided.

2.2 Lighthill-Curle theory of aerodynamic sound

A mathematically formulated linkage between description of fluid flow and sound generation phenomena was proposed and solved by M. J. Lighthill. His work [1] focused on sound generation as a byproduct of airflow as distinct from sound generated by vibration of solids.

Consider a system with fluctuating flow occupying a very large volume of fluid, at which the non fluctuating part is at rest. Three mechanism of introducing kinetic energy to the system and transforming it to "acoustic energy" are following:

I By forcing a mass of the fluid in a fixed region to fluctuate, as in the loudspeaker diaphragm

II By forcing the momentum in fixed space to fluctuate or by forcing the rates of flux through a given control surface to vary, as in vibrating part of a machine (or after striking a tuning-fork)

III By forcing the rates of flux through a given control surface to vary, without the vibrating motion of solid boundaries, as in noise generated turbulence in flow.

Efficiency of transformation the kinetic energy do sound decreases down the list. First two phenomena are well established in current knowledge and were described in many sources. The research on sound generated aerodynamically starts (probably) with aforementioned work [2].

Lighthill proposes, that Reynolds momentum equation (derrived in chapter 3) already expresses that the momentum changes at exactly the same rate as if the medium was at rest under the combined action of real stresses and fluctuating Reynolds stresses. Uniform acoustic medium at rest experiences stresses only from variation of density proportional to the speed of sound squared. A Lighthill stress tensor is therefore introduced to describe the fluctuations of the fluid medium subject to acoustic stresses:

$$T_{ij} = \rho v_i v_j + P_{ij} - a_0^2 \rho \delta_{ij} \tag{2.1}$$

Term P_{ij} is the compression tensor defined as:

$$P_{ij} = (p - p_0)\delta_{ij} - \sigma_{ij} \tag{2.2}$$

where σ_{ij} is the stress tensor due to molecular viscosity defined by:

$$\sigma_{ij} \equiv \left[\mu \left(\frac{\partial \overline{u_i}}{\partial x_j} + \frac{\partial \overline{u_j}}{\partial x_i}\right)\right] - \frac{2}{3}\mu \frac{\partial \overline{u_l}}{\partial x_l}\delta_{ij} \tag{2.3}$$

Propagation of sound in fluid medium without external forces is presented by following governing equations:

$$\frac{\partial \rho}{\partial t} + \frac{\partial}{\partial x_i}\left(\rho v_i\right)) = 0 \tag{2.4}$$

$$\frac{\partial}{\partial t}\left(\rho v_i\right) + a_0^2 \frac{\partial \rho}{\partial x_i} = 0 \tag{2.5}$$

$$\frac{\partial^2 \rho}{\partial t^2} - a_0^2 \nabla^2 \rho = 0 \tag{2.6}$$

The equation 2.4 is the continuity equation for a compressible fluid, equation 2.5 is an approximate equation of momentum and equation 2.6 is established by eliminating the ρv_i term from the previous equations.

By implementing the T_{ij} tensor to the equations 2.4 thru 2.6, the following form is obtained:

$$\frac{\partial \rho}{\partial t} + \frac{\partial}{\partial x_i}\left(\rho v_i\right)) = 0 \tag{2.7}$$

$$\frac{\partial}{\partial t}\left(\rho v_i\right) + a_0^2 \frac{\partial \rho}{\partial x_i} = -\frac{\partial T_{ij}}{\partial x_j} \tag{2.8}$$

$$\frac{\partial^2 \rho}{\partial t^2} - a_0^2 \nabla^2 \rho = \frac{\partial^2 T_{ij}}{\partial x_i \partial x_j} \tag{2.9}$$

Therefore a term describing the fluctuations related to acoustic phenomena is now linked to the flow governing equations. It can now be assumed, that resolving fluid flow along with the appropriate stress, strain and deformation terms can be now used to asses the sound phenomena in the flow field.

Should the receiver of the acoustical signal be outside the computational domain, further investigation must be concluded. Consider an unbounded flow field with a fluctuating point source, so that mass $Q(x,t)$ is introduced to the system at point x and time t, with total rate of introduction of $q(t)$. The density field is than given by the equation:

$$\rho - \rho_0 = \frac{1}{4\pi a_0^2} \frac{q'\left(\frac{t-r}{a_0}\right)}{r} \tag{2.10}$$

where r is the distance from source and $q'(t)$ is the time derivative of $q(t)$ and is defined as instantaneous source strength. For distributed source the equation 2.10 takes form:

$$\rho - \rho_0 = \frac{1}{4\pi a_0^2} \int \frac{\partial}{\partial t} Q \left(y, t - \frac{|x-y|}{a_0} \right) \frac{dy}{|x-y|} \tag{2.11}$$

The equation 2.11 is then solved to a form:

$$\rho - \rho_0 = \frac{1}{4\pi a_0^2} \frac{\partial^2}{\partial x_i \partial x_j} \int T_{ij} \left(y, t - \frac{|x-y|}{a_0} \right) \frac{dy}{|x-y|} \tag{2.12}$$

The equation 2.12 considers an unbounded flow field with point or volumetric source of fluctuations considered as quadrupole sources of acoustic fluctuations. This concept was evolved by Curle [3] to include the effect of solid boundaries on their reflection and diffraction. The modification of the original equation 2.12 is:

$$\begin{aligned} \rho - \rho_0 = & \frac{1}{4\pi a_0^2} \frac{\partial^2}{\partial x_i \partial x_j} \int_V T_{ij} \left(y, t - \frac{r}{a_0} \right) \frac{dy}{r} \\ & - \frac{1}{4\pi a_0^2} \frac{\partial}{\partial x_i} \int_S P_i \left(y, t - \frac{r}{a_0} \right) \frac{dS(y)}{r} \end{aligned} \tag{2.13}$$

where:

$$P_i = -l_j P_{ij} \tag{2.14}$$

where: $l_i = (l_1, l_2, l_3) = n$ is the direction cosines of the outward normal from the fluid, and the sound generated in a medium at rest by a distribution of dipoles of strength P_i per unit area and therefore P_i is the force per unit area exerted on the fluid by the solid boundaries in the x_i direction.

2.3 FW-H Analogy

Further development of analogies developed in references [1], [2] and [3] is presented in work [4]. The extension to the theory includes the effect of arbitrary convective motion of fluid. More over, the FW-H analogy switches from Lighthill's unbounded fluid to a bounded volume. Thus it is possible co compute the flow phenomena within the acoustic near field (which in this case would be a CFD domain) and compute the sound propagation outwards to the acoustic far field (outside the CFD domain) using wave propagation equations.

FW-H analogy derives it's governing equation from a volume of fluid V enclosed by a surface Σ, divided into regions 1 and 2 with surface of the discontinuity S moving into region 2 with velocity v. By formulating the rate of change of mass within volume V and deriving a generalized continuity and momentum equations, an equation governing the generation and propagation of sound is obtained.

$$\left(\frac{\partial^2}{\partial t^2} - a^2\frac{\partial^2}{\partial x_i^2}\right)\left(\overline{\rho - \rho_0}\right) = \frac{\partial^2 \overline{T_{ij}}}{\partial x_i \partial x_j} - \frac{\partial}{\partial x_i}\left(P_{ij}\delta(f)\frac{\partial f}{\partial x_j}\right) + \frac{\partial}{\partial t}\left(\rho_0 v_i \delta(f)\frac{\partial f}{\partial x_i}\right) \tag{2.15}$$

where: $(\overline{\rho - \rho_0})$ is the generalized density perturbation - the amplitude of sound and $\overline{T_{ij}}$ is equal to T_{ij} (eq. 2.1) outside any surfaces and equal 0 when within them. Equation $f = 0$ defines the division surface surface S, such that $f < 0$ is in the region 1 and $f > 0$ in region 2 (Heavyside function). The $\delta(f)$ is the Dirac delta function.

The equation 2.15 shows that sound can be regarded as generated by three source distributions: in volume - the quadrupole distribution of strength T_{ij}, on surface - the distribution of dipoles of strength density $P_{ij}n_j$ and monopole distributions from the displacement of volume by the moving surface.

Equation 2.15 can be rewritten to a different form:

$$\begin{aligned}\frac{1}{a_0^2}\frac{\partial^2 (p')}{\partial t^2} - \nabla^2 (p') &= \frac{\partial^2}{\partial x_i \partial x_j}\{T_{ij}H(f)\} \\ &-\frac{\partial}{\partial x_i}\{[P_{ij}n_j + \rho u_i (u_n - v_n)]\,\delta(f)\} \\ &+\frac{\partial}{\partial t}\{[\rho_0 v_n + \rho (u_n - v_n)]\,\delta(f)\}\end{aligned} \tag{2.16}$$

where:

$p' = p - p_0$ — sound pressure fluctuation

u_i — fluid velocity in the x_i direction

u_n — fluid velocity component normal to the surface $f = 0$

v_i — surface velocity in the x_i direction

v_n — surface velocity component normal to the surface

$H(f)$ — Heavyside function

$\delta(f)$ — Dirac delta function

The rewritten equation 2.16 represents an inhomogeneous wave equation can be integrated under specific assumptions and the solutions consists of surface (mono-pole and dipole sources) and volume integrals (quadrupole sources). Software package used for further computations ommits the effect of volume integral, therefore the result is of following form:

$$p'(x,t) = p'_T(x,t) + p'_L(x,t) \tag{2.17}$$

with further development of the solution:

$$\begin{aligned} 4\pi p'_T(x,t) = \int\limits_{f=0} \left[\frac{\rho_0 \left(\dot{U}_n + U_{\dot{n}} \right)}{r\left(1-M_r\right)^2} \right] dS \\ + \int\limits_{f=0} \left[\frac{\rho_0 U_n \{ r\dot{M}_r + a_0 \left(M_r - M^2 \right) \}}{r^2 \left(1-M_r\right)^3} \right] dS \end{aligned} \tag{2.18}$$

$$\begin{aligned} 4\pi p'_L(x,t) = \frac{1}{a_0} \int\limits_{f=0} \left[\frac{\dot{L}_r}{r\left(1-M_r\right)^2} \right] dS \\ + \int\limits_{f=0} \left[\frac{L_r - L_M}{r^2\left(1-M_r\right)^2} \right] dS \\ + \frac{1}{a_0} \int\limits_{f=0} \left[\frac{L_r \{ r\dot{M}_r + a_0 \left(M_r - M^2 \right) \}}{r^2 \left(1-M_r\right)^3} \right] dS \end{aligned} \tag{2.19}$$

where:

$$U_i = v_i + \frac{\rho}{\rho_0} \left(u_i - v_i \right) \tag{2.20}$$

$$L_i = P_{ij} n_j + \rho v_i \left(u_i - v_i \right) \tag{2.21}$$

When the integration surface coincides with an impenetrable wall, the two terms equation 2.17, $p'_T(x,t)$ and $p'_L(x,t)$ are often referred to as thickness and loading terms, respectively, in light of their physical meanings. The square brackets in equations 2.18 and 2.19 denote that the kernels of the integrals are computed at the corresponding retarded times, τ, defined as in equation 2.22, given the receiver time, t, and the distance to the receiver, r.

$$\tau = t - \frac{r}{a_0} \tag{2.22}$$

The various subscripted quantities appearing in equations 2.18 and 2.19 are the inner products of a vector and a unit vector implied by the subscript. For instance, $L_r = \vec{L} \cdot \vec{r} = L_i r_i$ and $U_n = \vec{U} \cdot \vec{n} = U_i n_i$, where $\vec{r}$ and $\vec{n}$ denote the unit vectors in the radiation and wall-normal directions, respectively. The Mach number vector M_i in equations 2.18 and 2.19 relates to the motion of the integration surface: $M_i = \dfrac{v_i}{a_0}$. The L_i quantity is a scalar product $L_i M_i$. The dot over a variable denotes source-time differentiation of that variable [5] [4] [6].

FW-H analogy is therefore the general form of Lighthill's acoustic analogy for aerodynamically generated noise, including volume sources of quadrupole kind, such as turbulence in free stream, and dipole and monopole sources of the moving solid body surface within the flow. Solution of the governing equation 2.15 given in equations 2.17, 2.19 & 2.18 ommits the sources as weak.

2.4 Limitations to acoustic analogies

Hybrid methods, including the presented Ffowks Williams – Hawking analogy provide a computationally efficient task for engineering problems such as air frame noise, jet injection to atmosphere noise (that is jet engine noise problem), effect of wake generated by automobile mirror on noise in the vehicle cabin. The solution to the FW-H governing equation presented in equations 2.18 and 2.19 may reach instability when the Mach number in the sound radiation direction M_r approaches 1, that is: when the freestream flow velocity approaches sonic conditions. Using the hybrid approach with acoustic analogies may be challenging and pose risk of obtaining "non-physical" results for case considered in this thesis, that is blade of axial compressor in stationary reference frame.

For phenomena characteristic to axial compressor flow, that is strong shock waves, shock wave with boundary layer interaction, high separation of flow enforced by shock waves, and mostly, high adverse pressure gradient may cause mathematical and numerical instabilities to the solution. Considering the pressure change within the computational domain, or, from the governing equation's standpoint, the volume enclosed by a surface, poses some difficulty to choosing free-stream values of density and pressure.

Further attempts towards gaining insight of the sound generation phenomena shall be performed by attempting to use a direct formulation of such.

Chapter 3

Approach and direct formulation of noise analysis

3.1 Direct formulation of noise analysis

The intention behind this study is to perform a flow field noise analysis in CFD without implementation of acoustical analogies to the CFD code itself. Moreover, very limited information on direct formulation of noise analysis was found during the research, with even fewer research on acoustical near field of transonic axial compressors or axial fans of twin spool jet engines.

The process for the direct formulation noise analysis is following:

1. Obtain raw flow field data of static pressure, velocity magnitude from CFD analysis.
2. Perform averaging over time of pressure and velocity magnitude for each point or cell in the flow field (equation 3.1).
3. Obtain offset from mean static pressure and velocity magnitude for every timestep for every point/cell in the saved flow field (equation 3.2).

$$\bar{p} = \frac{1}{n}\sum_{n=1}^{N} p_k \qquad and \qquad \bar{u} = \frac{1}{n}\sum_{n=1}^{N} u_k \tag{3.1}$$

$$p_{n\ sound} = p_n - \bar{p} \qquad and \qquad u_{n\ particle} = u_n - \bar{u} \tag{3.2}$$

Sound pressure signal and flow velocity offset is obtained for every node or cell centroid throughout the simulation flowtime. This dataset can be now post processed. Dataset obtained in described manner now contains sound pressure of the flow field in every mesh node or cell centroid throughout the computational time. The dataset is now post processed to obtain quantity information of the acoustic nearfield.

Sound intensity for cells/nodes in fluid volume is calculated using formula 3.3.

$$I_n = p_{n\ sound} \cdot u_{n\ particle} \tag{3.3}$$

RMS sound pressure level and intensity level can be obtained from the respective data with use of the formula 3.4.

$$p_{rms} = \sqrt{\frac{\sum_{n=1}^{N} p_{n\ sound}^2}{N}} \qquad I_{rms} = \sqrt{\frac{\sum_{n=1}^{N} u_{n\ particle}^2}{N}} \tag{3.4}$$

Sound pressure decibel level (SPLdB) for time specific $p_{k\ sound}$ values and and RMS values p_{rms} is computed using formula 3.5 with standard reference pressure $p_{ref} = 20\mu Pa$, whereas for sound intensity with formula 3.6 and with reference intensity $I_{ref} = 1pW/m^2$.

$$SPLdB = 20 \cdot \log_{10}\left(\frac{|p_{n\ sound}|}{p_{ref}}\right) \tag{3.5}$$

$$SILdB = 10 \cdot \log_{10}\left(\frac{|I_n|}{I_{ref}}\right) \tag{3.6}$$

The signal obtained by direct approach is stored in discrete time samples, therefore using a continuous Fourier Transform would require approximation of the sampled signal to a continuous function, which for large datasets is unjustified. In order to obtain ordinary sinuses of the acoustic signal a Discrete Fourier Transform is performed (eq. 3.7).

$$X_k = \sum_{n=0}^{N-1} x_n \cdot e^{-\frac{j2\pi kn}{N}} \tag{3.7}$$

Let's assume that:

$$b_n = \frac{2\pi kn}{N} \tag{3.8}$$

Therefore, the equation 3.7 can be written as:

$$X_k = x_0 e^{-jb_0} + x_1 e^{-jb_1} + x_2 e^{-jb_2} + \ldots + x_n e^{-jb_{N-1}} \tag{3.9}$$

Using Euler's identity the exponent is decomposed (eq. 3.10) to a complex sum:

$$e^{jx} = \cos(x) + j \cdot \sin(x) \tag{3.10}$$

Therefore the equation 3.7 can be written as:

$$X_k = x_0[\cos(-b_0) + j\sin(-b_0)] + \ldots + x_n[\cos(-b_{N-1}) + j\sin(-b_{N-1})] \tag{3.11}$$

Rearranging the equation 3.11 and summing up the real and imaginary components will return a complex vector X_k for "k-th" frequency bin.

$$X_k = A_k + jB_k \tag{3.12}$$

The frequency resolution of the DFT depends on the sampling frequency and number of samples, and is calculated by formula 3.13.

$$f_{bin} = \frac{f_{sample}}{N} \tag{3.13}$$

Fourier coefficients are then used to compute the magnitude (eq. 3.14) and phase shift (eq. 3.15) for the "k-th" frequency bin ordinary sinus.

$$Mag_k = 2 \cdot \sqrt{A_k^2 + B_k^2} \cdot \frac{1}{N} \tag{3.14}$$

$$\theta_k = \arctan \frac{B_k}{A_k} \tag{3.15}$$

3.2 CFD analysis requirements

References [1], [2], [4] and [3] provide a theoretical insight on generating sound in fluid flow due to shear mixing of flows or by implementing a solid boundary in the flow. General remark is: any source of turbulence that result in pressure fluctuation will result in generating sound. Therefore the main requirement for used CFD code for direct noise analysis is the capability of resolving turbulent flow and corresponding fluctuations of the pressure.

Let's consider the effect of injection of energy to the fluid resulting in creation of eddies (Fig. 3.1)

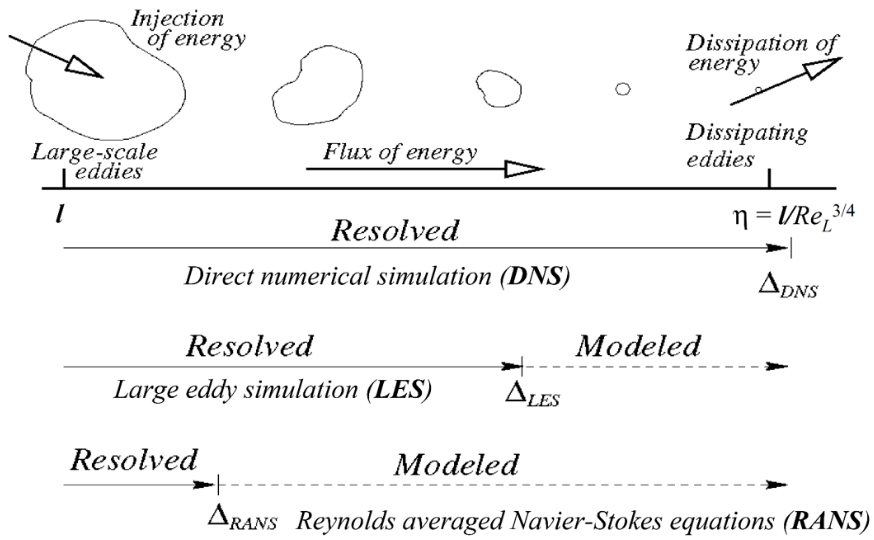

FIGURE 3.1: Resolving eddies in different kinds of CFD analyses

3.2.1 Govering equations

Continuity equation:

$$\frac{\partial \rho}{\partial t} + \nabla(\rho U) = 0 \tag{3.16}$$

Momentum equation:

$$\frac{dU}{dt} = -\frac{1}{\rho}\nabla p + \nu \nabla^2 U \tag{3.17}$$

3.2.2 Direct Numerical Simulation

Considering the direct formulation of noise, the Direct Numerical Simulation is seemingly the best tool of choice. The DNS formulation of flow solves directly the discrete form of Navier-Stokes Equation without any turbulence models. Size limit of the resolved eddies is the Kolmogorov limit (eq. 3.18). In order to properly resolve the DNS simulation op to this scale, the mesh sizing must be at least as small as the expected Kolmogorov limit at given Reynolds number.

$$\eta \approx \frac{l}{Re^{3/4}} \tag{3.18}$$

Reference [7] provides information on calculating the mesh grid node count for DNS calculations (eq. 3.19) for flat plate airfoil of aspect ratio L_z/L_x. The computational box for this case is of size $L_x \times \delta \times L_z$ in streamwise, normal to plate and spanwise direction respectively, where δ is the boundary layer thickness.

$$N_{DNS} = 0.000153 \frac{L_z}{L_x} Re_{L_x}^{37/14} \left[1 - \left(\frac{Re_{x_0}}{Re_{L_x}} \right)^{23/14} \right] \tag{3.19}$$

Point x_0 is the location where formulas 3.20 and 3.21 are valid for Reynolds number range ($10^6 \leq Re_x \leq 10^9$).

$$\delta = x \cdot 0.16 Re_x^{(-1/7)} \tag{3.20}$$

$$c_f = 0.027 Re_x^{(-1/7)} \tag{3.21}$$

For aspect ratio $L_z/L_x = 4$ and $Re_{x_0} = 5 \cdot 10^5$ the node count for streamwise $Re = 10^6$ is roughly $2.99 \cdot 10^{12}$ nodes and for $Re = 10^7$ is roughly $1.92 \cdot 10^{15}$ nodes.

Such node and cell counts are impossible to solve within practical walltime, therefore usage of DNS for sound analysis is limited to small Reynolds numbers.

3.2.3 Large Eddy Simulation

Large eddy simulation (LES) is a mathematical model for turbulence used in computational fluid dynamics. It was initially proposed in 1963 by Joseph Smagorinsky to simulate atmospheric air currents [8].

The principal idea behind LES is to reduce the computational cost by ignoring the smallest length scales, which are the most computationally expensive to resolve, via low-pass filtering of the Navier–Stokes equations. Such a low-pass filtering, which can be viewed as a time- and spatial-averaging, effectively removes small-scale information from the numerical solution. This information is not irrelevant, however, and its effect on the flow field must be modeled, a task which is an active area of research for problems in which small-scales can play an important role such as acoustics [9].

The governing equations employed for LES are obtained by filtering the time dependent Navier-Stokes equations in either Fourier (wave-number) space or configuration (physical) space. The filtering process effectively filters out the eddies whose scales are smaller than the filter width or grid spacing used in the computations. The resulting equations therefore govern the dynamics of large eddies [5].

A filtered variable is defined by:

$$\overline{\phi}(x) = \int\limits_D \phi\left(x'\right) G\left(x, x'\right) dx' \tag{3.22}$$

where D is the fluid domain, and G is the filter function that determines the scale of the resolved eddies. The finite volume discretization itself implicitly provides the filtering operation:

$$\overline{\phi}(x) = \frac{1}{V} \int_{\nu} \phi\left(x'\right) dx', \; x' \in \nu \tag{3.23}$$

where V is the volume of a computational cell. The filter function, $G(x, x')$ implied here is then:

$$G(x, x') = \begin{cases} \frac{1}{V}, & \text{if } x' \in \nu \\ 0, & \text{otherwise} \end{cases} \tag{3.24}$$

For compressible flows, it is convenient to introduce the density-weighted (or Favre) filtering operator:

$$\tilde{\phi} = \frac{\overline{\rho\phi}}{\overline{\phi}} \tag{3.25}$$

Filtering the continuity 3.16 and momentum 3.17 equations following form is obtained:

$$\frac{\partial \rho}{\partial t} + \frac{\partial}{\partial x_i}\left(\rho \overline{u_i}\right) = 0 \tag{3.26}$$

$$\frac{\partial}{\partial t}\rho\overline{u_i} + \frac{\partial}{\partial x_j}\left(\rho\overline{u_i u_j}\right) = \frac{\partial}{\partial x_j}\left(\sigma_{ij}\right) - \frac{\partial \overline{p}}{\partial x_i} - \frac{\partial \tau_{ij}}{\partial x_j} \tag{3.27}$$

where σ_{ij} is the stress tensor due to molecular viscosity defined by:

$$\sigma_{ij} \equiv \left[\mu\left(\frac{\partial \overline{u_i}}{\partial x_j} + \frac{\partial \overline{u_j}}{\partial x_i}\right)\right] - \frac{2}{3}\mu\frac{\partial \overline{u_l}}{\partial x_l}\delta_{ij} \tag{3.28}$$

and τ_{ij} is the subgrid-scale stress defined by:

$$\tau_{ij} \equiv \rho\overline{u_i u_j} - \rho\overline{u_i}\,\overline{u_j} \tag{3.29}$$

The Favre Filtered Navier-Stokes equation takes the same form as equation 3.27. The compressible form of the subgrid stress tensor is defined as:

$$\tau_{ij} = \overline{\rho}\widetilde{u_i u_j} - \overline{\rho}\tilde{u_i}\,\tilde{u_j} \tag{3.30}$$

The subgrid-scale stresses resulting from the filtering operation are unknown, and require modeling. The subgrid-scale turbulence models employ the Boussinesq hypothesis [10] in the RANS models, computing subgrid-scale turbulent stresses from:

$$\tau_{ij} - \frac{1}{3}\tau_{kk}\delta_{ij} = -2\mu_t \overline{S_{ij}} \tag{3.31}$$

where μ_t is the subgrid-scale turbulent viscosity. The isotropic part of the subgrid-scale stresses τ_{kk} is not modeled, but added to the filtered static pressure term. S_{ij} is the rate-of-strain tensor for the resolved scale defined by:

$$\overline{S_{ij}} \equiv \frac{1}{2}\left(\frac{\partial \overline{u_i}}{\partial x_j} + \frac{\partial \overline{u_j}}{\partial x_i}\right) \tag{3.32}$$

Equation 3.30 is split into its isotropic and deviatoric parts:

$$\tau_{ij} - \frac{1}{3}\tau_{kk}\delta_{ij} = -2\mu_t \left(S_{ij} - \frac{1}{3}S_{kk}\delta_{ij}\right) \tag{3.33}$$

Using LES approach is viable for resolving directly formulated noise, yet the computational cost of such calculations is still relatively large due to mesh sizing requirements. As stated by [7] the required node count for the analysis can be described by formulas 3.34 and 3.35 for modeled and resolved boundary layers.

$$N_{wm} = 54.7\frac{L_z}{L_x} n_x n_y n_z Re_{L_x}^{2/7}\left[\left(\frac{Re_{L_x}}{Re_{x_0}}\right)^{(5/7)} - 1\right] \tag{3.34}$$

$$N_{wr} = 0.021\frac{n_y}{\Delta x_w^+ \Delta z_w^+}\frac{L_z}{L_x} Re_{L_x}^{13/7}\left[1 - \left(\frac{Re_{L_x}}{Re_{x_0}}\right)^{(6/7)}\right] \tag{3.35}$$

The computational box for this case is of size $L_x \times \delta \times L_z$ in streamwise, normal to plate and spanwise direction respectively, where δ is the boundary layer thickness.

For $L_z/L_x = 4$ and $Re_{x_0} = 5 \cdot 10^5$ the node count for streamwise $Re = 10^6$ and $Re = 10^7$ is computed. The $n_x n_y n_z$ product is the number of grid points to resolve the cubic computational volume δ^3 exterior to the viscous wall region. Suggested value of $n_x n_y n_z = 2500$, where $n_x = 10$ $n_y = 25$ $n_z = 10$ was used for the computation of node count with equation 3.34. Suggested $\Delta x_w^+ \approx 100$, $\Delta z_w^+ \approx 20$ and $n_y \approx 10$ was used for computation of node count with equation 3.35.

Node count for $Re = 10^6$ is roughly $1.82 \cdot 10^7$ nodes for modelled and $2.61 \cdot 10^7$ nodes for resolved wall flow. For $Re = 10^7$ the figures are $4.10 \cdot 10^8$ and $3.88 \cdot 10^9$ nodes respectively [7].

It must be noted that provided cell count is solely for a flow box of boundary layer width. Respective mesh sizing should be propagated towards volume of the computational domain thus enlarging the mesh even further.

LES analyses are commonly used in research and engineering and the method used is feasible for the direct noise formulation. However the computational expense of running such cases is high, but manageable. Second limiting factor for LES is the amount of data generated during the process. As the direct approach requires storing at least every second time step for further processing, terabytes of data are predicted.

3.2.4 Reynolds Averaged Navier Stokes

The most computationally efficient method for resolving turbulent flows is using Reynolsds Averaged Navier Stokes equation. Consider a conservation variable ϕ of fluid described by spatial and temporal variables. The quantity may be decomposed to a sum of time averaged value in given spatial coordinates and time dependent fluctuations (eq. 3.36).

$$\phi(x,y,z,t) = \overline{\phi(x,y,z,t)} + \phi'(x,y,z,t) \tag{3.36}$$

Consider at first the continuity equation 3.16. By applying Reynolds decomposition to velocity vector we obtain:

$$\frac{\partial \rho}{\partial t} + \frac{\partial \rho \overline{u_i}}{\partial x_i} + \frac{\partial \rho u_i'}{\partial x_i} = 0 \tag{3.37}$$

By averaging the both sides of the equation 3.37 and applying averaging rules to its components we obtain:

$$\frac{\partial \rho}{\partial t} + \frac{\partial \overline{\rho \overline{u_i}}}{\partial x_i} + \frac{\partial \overline{\rho u_i'}}{\partial x_i} = 0 \tag{3.38}$$

Because the average of an average is equal average, and the average of the fluctuation component is equal 0 we obtain equation 3.39, the Reynolds averaged continuity equation.

$$\frac{\partial \rho}{\partial t} + \frac{\partial \rho \overline{u_i}}{\partial x_i} = 0 \tag{3.39}$$

By taking the momentum equation 3.17, switching to the index notation and applying the Reynolds decomposition we obtain the equation 3.40

$$\underbrace{\frac{\partial\left(\overline{u_i}+u_i'\right)}{\partial t}}_{1}+\underbrace{\left(\overline{u_j}+u_j'\right)\frac{\partial\left(\overline{u_j}+u_j'\right)}{\partial x_j}}_{2}=\underbrace{-\frac{1}{\rho}\frac{\partial\left(\overline{p}+p'\right)}{\partial x_i}}_{3}+\underbrace{\nu\frac{\partial^2\left(\overline{u_i}+u_i'\right)}{\partial x_j^2}}_{4} \tag{3.40}$$

Components 1, 3 and 4 of the above equation are treated in the same manner as the continuity equation and thus we obtain:

$$\underbrace{\frac{\partial\overline{u_i}}{\partial t}}_{1} \qquad \underbrace{\frac{1}{\rho}\frac{\partial\overline{p}}{\partial x_i}}_{3} \qquad \underbrace{\nu\frac{\partial^2\overline{u_i}}{\partial x_j^2}}_{4} \tag{3.41}$$

The decomposition of component 2 from the equation 3.40 requires multiplication of the components within the braces and performing Reynolds averaging on each of the products:

$$\underbrace{\overline{\left(\left(\overline{u_j}+u_j'\right)+\frac{\partial\left(\overline{u_i}+u_i'\right)}{\partial x_j}\right)}}_{2}=\underbrace{\overline{\left(\overline{u_j}\frac{\partial\overline{u_i}}{\partial x_j}\right)}}_{\mathrm{M}\cdot\mathrm{M}\neq 0}+\underbrace{\overline{\left(\overline{u_j}\frac{\partial u_i'}{\partial x_j}\right)}}_{\mathrm{M}\cdot\mathrm{F}=0}+\underbrace{\overline{\left(u_j'\frac{\partial\overline{u_i}}{\partial x_j}\right)}}_{\mathrm{F}\cdot\mathrm{M}=0}+\underbrace{\overline{\left(u_j'\frac{\partial u_i'}{\partial x_j}\right)}}_{\mathrm{F}\cdot\mathrm{F}\neq 0} \tag{3.42}$$

The $\mathrm{F}\cdot\mathrm{F}\neq 0$ product can be further simplified by equation:

$$\frac{\partial u_j'u_i'}{\partial x_j}=\underbrace{u_j'\frac{\partial u_j'}{\partial x_j}}_{=0}+\underbrace{u_j'\frac{\partial u_i'}{\partial x_j}}_{\mathrm{F}\cdot\mathrm{F}\neq 0} \tag{3.43}$$

By inserting the components 1 through 4 from equations 3.41 and 3.42 modified by equation 3.43 to the equation 3.40 we obtain the Reynolds averaged momentum equation:

$$\frac{d\overline{U}}{dt}=-\frac{1}{\rho}\frac{\partial\overline{p}}{\partial x_i}+\frac{\partial}{\partial x_j}\left[\nu\frac{\partial\overline{u_j}}{\partial x_j}-\overline{u_i'u_j'}\right] \tag{3.44}$$

By representing the viscous terms as a stress tensor (eq. 3.45) we obtain the momentum equation with turbulent stress (eq 3.46)

$$\nu\frac{\partial^2\overline{u_i}}{\partial x_j^2}=\frac{1}{\rho}\frac{\partial}{\partial x_j}\tau_{ij} \tag{3.45}$$

$$\frac{d\overline{U}}{dt}=-\frac{1}{\rho}\nabla\overline{p}+\frac{1}{\rho}\frac{\partial}{\partial x_j}\left[\tau_{ij}-\rho\overline{u_i'u_j'}\right] \tag{3.46}$$

The $\rho\overline{u_i'u_j'}$ term can be further transformed to Reynolds stress tensor linked to shear stress. The remaining fluctuating component is then modeled rather than resolved, by one of many turbulence model based on Bousinessque theory.

3.2.5 Hybrid RANS/LES Methods

At first, the concepts of Reynolds Averaging and Spatial Filtering seem incompatible, as they result in different additional terms in the momentum equations (Reynolds Stresses and sub-grid stresses). This would preclude hybrid models like Scale-Adaptive Simulation (SAS), Detached Eddy Simulation (DES), Shielded DES (SDES), or Stress-Blended Eddy Simulation (SBES), which are based on one set of momentum equations throughout the RANS and LES portions of the domain. However, it is important to note that once a turbulence model is introduced into the momentum equations, they no longer carry any information concerning their derivation (averaging). Case in point is that the most popular models, both in RANS and LES, are eddy viscosity models that are used to substitute either the Reynolds- or the sub-grid stress tensor. After the introduction of an eddy viscosity (turbulent viscosity), both the RANS and LES momentum equations are formally identical. The difference lies exclusively in the size of the eddy-viscosity provided by the underlying turbulence model. This allows the formulation of turbulence models that can switch from RANS to LES mode, by lowering the eddy viscosity in the LES zone appropriately, without any formal change to the momentum equations [5].

For further calculations, Delayed Detached Eddy Simulation with $SSTk-\omega$ model was chosen. In the DES approach, the unsteady RANS models are employed in the boundary layer, while the LES treatment is applied to the separated regions. The LES region is normally associated with the core turbulent region where large unsteady turbulence scales play a dominant role. In this region, the DES models recover LES-like subgrid models. In the near-wall region, the respective RANS models are recovered [5].

Formulation of DES is the development of the Spalart-Allmaras turbulence model for RANS formulation [11], therefore the theoretical formulations are derived from the S-A model.

The S-A model uses modified turbulent viscosity $\tilde{\nu}$ in place of the turbulent kinematic viscosity.

$$\frac{\partial}{\partial t}(\rho\tilde{\nu})+\frac{\partial}{\partial x_i}(\rho\tilde{\nu}u_i)=G_\nu+\frac{1}{\sigma_{\tilde{\nu}}}\left[\frac{\partial}{\partial t}\left\{(\mu+\rho\tilde{\nu})\frac{\partial\tilde{\nu}}{\partial x_j}\right\}+C_{b2}\rho\left(\frac{\partial\tilde{\nu}}{\partial x_j}\right)^2\right]-Y_\nu+S_{\tilde{\nu}} \quad (3.47)$$

Turbulence production G_ν and destruction Y_ν terms are modeled as:

$$G_\nu = C_{b1}\rho\tilde{S}\tilde{\nu} \tag{3.48}$$

$$Y_\nu = C_{wq}\rho f_w \left(\frac{\tilde{\nu}}{d}\right)^2 \tag{3.49}$$

Where d is the length scale calculated as the distance to the closest wall and $\tilde{S}$ being the measure of deformation tensor:

$$\tilde{S} \equiv S + \frac{\tilde{\nu}}{\kappa^2 d^2} f_{v2} \tag{3.50}$$

where:

$$S \equiv |\Omega_{ij}| + C_{prod}\min\left(0, |S_{ij}| - |\Omega_{ij}|\right) \tag{3.51}$$

where:

$$C_{prod} = 2.0,\ |\Omega_{ij}| \equiv \sqrt{2\Omega_{ij}\Omega_{ij}},\ |S_{ij}| \equiv \sqrt{2S_{ij}S_{ij}} \tag{3.52}$$

with the mean strain rate defined as:

$$S_{ij} = \frac{1}{2}\left(\frac{\partial u_j}{\partial x_i} + \frac{\partial u_i}{\partial u_j}\right) \tag{3.53}$$

The equation 3.49 shows that $\tilde{\nu}$ is proportional to the local deformation rate and wall distance: $\tilde{\nu} \propto Sd^2$. Smagorinsky model for "Sub-Grid-Scale" (SGS) scales the turbulent viscosity with local deformation and grid spacing: $\tilde{\nu} \propto S\Delta^2$.

By replacing the d in the S-A destruction term (eq. 3.49) with $\tilde{d}$:

$$\tilde{d} \equiv \min\left(d, C_{DES}\Delta\right) \tag{3.54}$$

a single model is obtained, acting as RANS with S-A turbulence modeling in regions where $d \ll \Delta$ and with LES behavior where $d \gg \Delta$. Grid spacing Δ is defined as the largest dimension of the computational cell $\Delta \equiv \max\left(\Delta x, \Delta y, \Delta z\right)$. In case of an ambiguous grid definition, where $\Delta < \delta$ the DES limiter can activate the LES mode inside the boundary layer, where the grid is not fine enough to sustain resolved turbulence. Therefore, a new formulation [12] of DES is available to preserve the RANS mode throughout the boundary layer. This is known as the delayed option or DDES for delayed DES [5].

DES and DDES methods can be used with other RANS turbulence models. Further analyses presented in this thesis use a $k-\omega SST$ model. For hybrid model the dissipation of turbulent kinetic energy is modified:

$$Y_k = \rho \beta^* k \omega F_{DES} \tag{3.55}$$

where:

$$F_{DES} = \max\left(\frac{L_t}{C_{DES}\Delta_{max}}\left(1 - F_{SST}\right), 1\right) \tag{3.56}$$

where C_{DES} is a calibration constant used in the DES model and has a value of 0.61, with $F_{SST} = 0, F_1, F_2$ where F_1 and F_2 are the blending functions of the Baseline and $SSTk-\omega$ model. The turbulent length scale is the parameter that defines this RANS model:

$$F_{DES} = \max\left(\frac{L_t}{C_{DES}\Delta_{max}}, 1\right) \tag{3.57}$$

The F_{DDES} blending function is given by equation 3.57 with model constants $C_{d1} = 20$, $C_{d2} = 3$ and r_d as defined by eq. 3.59:

$$F_{DDES} = \tanh\left[\left(C_{d1} r_{d1}\right)^{C_{d2}}\right] \tag{3.58}$$

$$r_d = \frac{\nu_t + \nu}{\kappa^2 y^2 \sqrt{0.5\left(S^2 + \Omega^2\right)}} \tag{3.59}$$

3.3 Mesh sizing requirements

Let's assume a sinusoidal pressure fluctuation $y(t)$ (equation 3.60) of ordinary frequency of f and amplitude A moving through ambient medium, for more than 5 cycles at speed of sound 3.61. The mathematical and numerical methods for solving flow field described in section above are capable of computing such pressure fluctuation in a fine resolution mesh.

$$y(t) = A\sin(2\pi f t + \phi) \tag{3.60}$$

$$a = \sqrt{\kappa R T} \tag{3.61}$$

Both cell size and time step size are limited by the wave length, and therefore frequency of the discussed pressure fluctuation. The wavelength is calculated by formula 3.62.

$$\lambda = \frac{v}{f} \tag{3.62}$$

Considered fluctuation travels through the finite volumes in the stationary CFD mesh. Pressure value is measured at the cell center for each timestep. At this stage, it is assumed that timestep is "good enough" for the analysis. Four possibilities are to be discussed

Scenario 1: wavelength is smaller than the edge length of the cell in the direction of propagation. In this condition, the pressure fluctuation performs a number of cycles within one cell (Fig. 3.2). Due to the numerical approach, such fluctuation will not be computed and recorded by data acquisition at the cell centroid or at node coordinates.

FIGURE 3.2: Scenario 1. Wavelength smaller than cell edge length

Scenario 2: wavelength and cell edge length in the direction of propagation are equal. In this condition, the pressure fluctuation performs one cycle within one cell in the direction of the fluctuation propagation (Fig. 3.3). Such pressure change will be also filtered out by the numerical scheme.

FIGURE 3.3: Scenario 2. Wavelength equal to cell edge length

Scenario 3: wavelength is equal to 4 minimum cell lengths in the direction of propagation. This is the minimum cell size condition for discussed approach. In this condition, the pressure fluctuation performs one cycle within four cells in the direction of the fluctuation propagation (Fig. 3.4). FVM method is now capable of computing the pressure resulting from sound wave propagation.

FIGURE 3.4: Scenario 3. Wavelength equal four minimum edge lengths

Scenario 4: wavelength is larger than 4 minimum cell edge lengths. In this condition, the pressure fluctuation performs one cycle within multiple cells in the direction of the fluctuation propagation (Fig. 3.5). FVM method computes pressure from the sound wave propagation across multiple cells.

FIGURE 3.5: Scenario 4. Wavelength larger than four minimum edge lengths

Based on these possibilities, the edge sizing of the finite volume cell should be at least four times smaller than the shortest wavelength expected in the flow field.

As there is no information on the pressure fluctuations in the flow field, the range of the further analyses will be limited to audible range of 20Hz to 20 000Hz. The wavelengths are calculated by formula 3.62 and divided by four to obtain the required cell sizing. The velocity of sound obtained by equation 3.61 with reference temperature $T = 300K$. The results for outermost sound frequencies of the audible range are presented in table 3.1

TABLE 3.1: Test case boundary conditions

Frequency [Hz]	Wave length [m]	Cell size [m]
20	17.390	4.347
20 000	0.01739	0.004347

3.4 Timestep requirements

There are two limiting factors for timestep requirements. The high frequency signal is limited by the timestep size, whereas the low frequencies are limited to the total number of timesteps and physical flow time calculated. The timestep size is calculated first.

Once sizing of the mesh is established, time at which the fluctuation passes the cell is established by simple formula 3.63. Distance s is the cell edge sizing, obtained as in section 3.3 and the relation between cell size and wave length is presented in equation 3.65.

$$a = \frac{s}{t} \tag{3.63}$$

Where

$$t = \frac{1}{f} \tag{3.64}$$

$$s = \frac{\lambda}{4} \tag{3.65}$$

By rearranging the equation 3.63 to solve for t and substituting λ by 3.62 we obtain:

$$t = \frac{s}{a} = \frac{\lambda}{4a} = \frac{a}{f} \cdot \frac{1}{4a} = \frac{1}{4f} \tag{3.66}$$

Time step t becomes also a sampling frequency for the pressure signal therefore it must be compared with the requirements stated by Shannon-Nyquist-Whitaker theorem: *If a function x(t) contains no frequencies higher than B hertz, it is completely determined by giving its ordinates at a series of points spaced 1/(2B) seconds apart.* Presented time stepping approach fulfills that theorem.

Equation 3.66 shows that time step for the analysis is dependent from the expected value of high frequency fluctuations.

In order to capture frequencies on the low end of the spectrum, the analysis must be performed long enough to capture at least a single, with optimum 5 or more periods, of the desired low frequency. Assuming lower end of the audible frequency spectrum, the 20Hz frequency, the simulation time must resemble at least 0.05s of flow time with optimum 0.25s of flow time at given timestep.

3.5 Limiting factors of the direct approach

Described direct formulation noise analysis is solely a post processing approach relying on data generated on CFD analysis. In order to obtain reasonable results down the process, the analysis itself mus be capable of delivering pressure fluctuations that can be considered as acoustic in source.

It is advised to used a turbulence model that is capable of resolving small scale turbulence on a mesh that will allow such resolution. Utilizing LES formulation or at least hybrid RANS/LES turbulence model such as DDES. Using an averaging formulation such as RANS will cut off all of the fluctuations and is not suitable for this approach.

The range of frequencies captured by this method depends on the mesh sizing and timestep sizing. Therefore, if the range of expected frequencies is known or at least estimated, the mesh sizing and timestep size can be adjusted for the given case. For analysis within audible range, 4000 timesteps are required for one 20Hz period. Considering the mesh sizing requirements, the mesh cell count will rise up to tens of millions for a single passage axial compressor blade. This makes the case files and storing data for each timestep relatively challenging and requires securing adequate storage beforehand.

A major limiting factor is the implementation of the direct noise formulation post-processing. For this thesis, the method was implemented in python v.3.5 high level programming language. Python code is written in C/C++ and provides a vast array of additional libraries for handling files, tabular data and performing mathematical operations. The code is presented in appendices to this dissertation. Although easy to implement, python code is known to be inefficient and slow while managing large amounts of data. Tools and algorithms used in implementing the averaging, obtaining sound pressure and particle velocity as well as DFT are build in tools from specific libraries. As convenient for the implementation, the post-processing code requires some amount of operational memory and disk space for generating the results.

The programming language used for the post-processing of data must be capable of generating 2D and 3D plots for visualization purposes. Ideally the processed and visualized data should resemble the mesh from which the initial data was gathered.

Chapter 4

Test case

4.1 NASA Rotor 67 transonic axial compressor

The test specimen for given analysis is a NASA Rotor 67 (R67) transonic axial compressor. Originating as a first stage of two stage fan for evaluation of design procedures, validation of experimental facilities as well as meshing and CFD tools. Both stages were used in a multitude of studies for aerodynamics, geometry optimisation, noise analyses and structural analyses. Full design procedure can be found in references [13] and [14]. The CFD analysis and further post processing of the pressure signals shall be performed on a single passage of a first stage rotor of the compressor. The setup for the calculations (apart from the single passage constraint) is relevant do case described in [15], which was the main source for geometry and flowfield data.

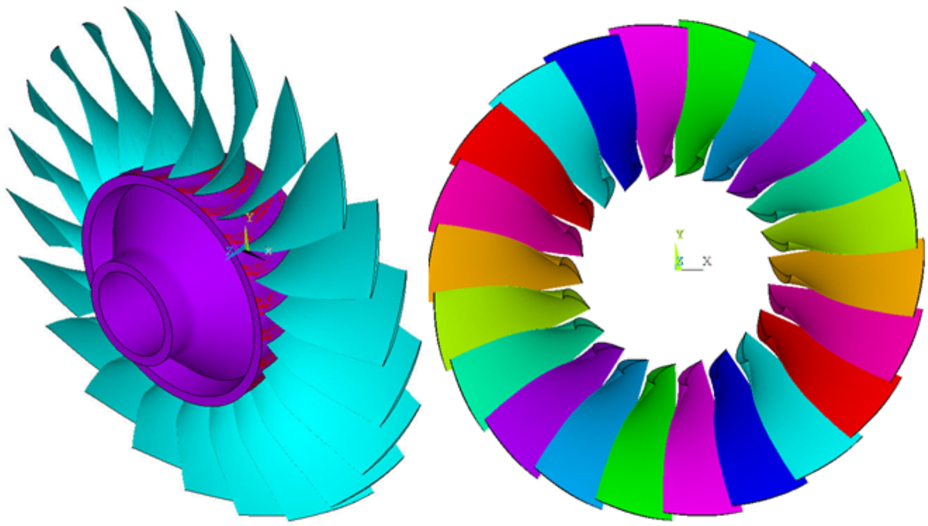

FIGURE 4.1: Geometry of NASA R67

Basic figures of the given rotor are, design pressure ratio of 1.63 at massflow of 33.25 kg/sec. The design rotational speed is 16 043 rpm, which yields a tip speed of 429 m/s and an inlet tip relative Mach number of 1.38. The rotor has 22 blades and an aspect ratio of 1.56 (based on average span/root axial chord). The inlet and exit tip diameters are 514 and 485 mm, respectively, and the inlet and exit hub/tip radius ratios are 0.375 and 0.478, respectively. A fillet radius of 1.78 mm is used at the airfoil-hub juncture. The square root of the mean square of the airfoil surface finish is 0.8 μm or better, the airfoil surface tolerance is $\pm$ 0.04 mm, and the running tip clearance is approximately 1.0 mm [15]. Surface roughness and some of the geometrical features are omitted during the preparation of the geometry and CFD mesh for reasons described in sections 4.2 and 4.3. General geometry of NASA R67 is presented on fig 4.1

4.2 3D geometry preparation

Geometry was prepared in Ansys ICEM 14.5 meshing software. Creating the geometry directly in the meshing software reduces the risk of creating flaws in the geometry, due to file translations. Mesh is created in millimeters.

The R67 blade coordinates for rotor and stator on both stages is given in references [13] and [14] and provide the blade elements in a Multiple-Circular-Arc fashion. In such approach the design blade elements lie on conical surfaces which approximate the actual stream flow surfaces. A blade-element-layout method is developed which preserves the constant-angle change characteristic of the circular-arc profile. More specifically, the mean camber line and the suction and pressure surface lines of a blade element are lines with a constant rate of angle change with path distance on a specified conical surface [16]. Although relatively comfortable for design purposes, such approach requires implementing a macro or script to desired CAD tool for creating the blade elements or transforming the MCA blade to Cartesian or cylindrical coordinates. Reference [16] provides an extended definition of MCA blade description as well as Fortran code for generating blade cross-section and geometric properties of the blade. Source [15] provides a list of coordinates for 14 profiles of the 1st stage rotor blade suction and pressure side, as well as coordinates for hub and casing int the meridional plane. These coordinates were used to create the geometry of the single passage of the subject blade. Coordinates are also available in Appendix D and project Github repository [17].

The coordinate system is a standard right-hand Cartesian CS. Rotation axis is set to Z-axis with flow in positive Z direction. The compressor rotation is set as in right-hand rule, the compressor rotates in clockwise direction when facing the blade leading edge. $Z = 0$ coordinate is defined by point number 1 on 1st blade design surface (see Appendix D for details).

Hub and casing flow path were created by importing formatted point data as a b-spline curve, followed by extrusion the curve to surface by rotating it by ±60°. Blade surfaces cylindrical coordinates were transformed to Cartesian coordinates using simple trigonometric calculations and imported as set of splines. Suction and pressure surface of the blade were created by lofting the surface along the imported splines. Leading and trailing edge radii were created in a similar manner with use of edge radius and edge tangency points given in [15]. Tip gap of the blade was created by offsetting the casing surface by 1.016 mm in the normal direction towards the rotation axis and creating a section line between blade surfaces and the offset surface.

Due to the estimated mesh cell count, only one blade passage is created, therefore a set of periodic surfaces must be defined. ICEM software is capable of creating a midline as an average of coordinates of two given lines. A midline was created for every design profile and was manually extended beyond the blade leading and trailing edge. Midlines were lofted to create a midsurface which was later on copied with rotation by $\pm 0.5 \cdot \frac{360°}{22}$ to create two identical periodic surfaces.

Aforementioned midlines were also rotated along Z-axis to create control surfaces for mesh stabilization and data acquisition down the process.

Reference [15] provides coordinates of hub and casing for the full experiment, however only a rotating part of the experimental rotor setup will be used. Two surfaces normal to Z direction at coordinates Z = -13.74 mm and Z = 93.65 mm are placed as inlet and outlet boundary conditions. Geometry was finished by necessary extrusions, trimming and other finishing operations to ensure high quality surface for meshing. Usually, the geometry must be watertight to ensure proper meshing process, however ICEM as patch-independent meshing software does not require that.

Physical experiment test compressor has a 1.78 mm fillet at airfoil-hub juncture. This feature was omitted as it would unnecessarily complicate the meshing process and increase the cell count.

Such approach allowed for creating a geometry for single blade passage with centered blade of 1st stage rotor of the test compressor (Fig 4.2).

4.3 Meshing approach

Following requisites are posed to the mesh for the discussed case:

- Possibly low number of elements fulfilling the mesh sizing requirements stated in chapter 3.1,
- Mesh should be a fully structural mesh including the tip gap,

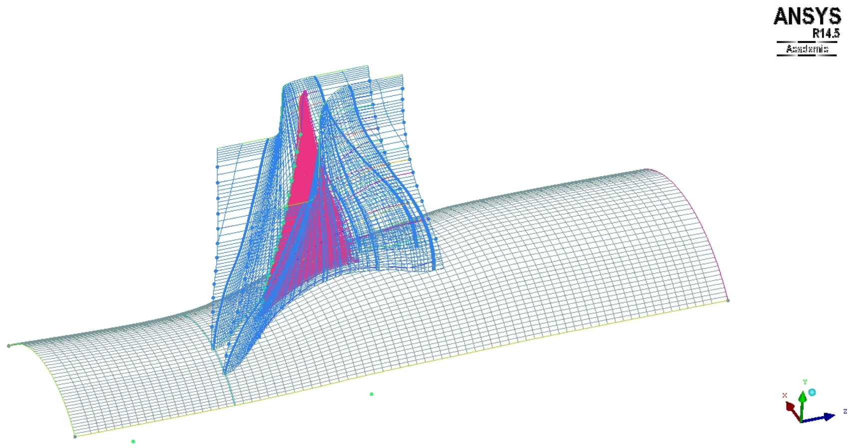

FIGURE 4.2: Final single passage geometry. Some features hidden for clarity

- The periodic boundary mesh must be identical/conforming for both boundaries,
- The mesh must have high quality metrics in terms of cell orthogonality and skew as defined by equations 4.1 & 4.2 respectively.

$$\text{Orthogonality} = \frac{\vec{A_i} \cdot \vec{f_i}}{|\vec{A_i}| \cdot |\vec{f_i}|} \tag{4.1}$$

$$\text{Skewness} = \frac{\text{Optimal Cell Size} - \text{Cell Size}}{\text{Optimal Cell Size}} \tag{4.2}$$

One of the initial mesh concepts was an unstructured mesh with triangular surface mesh extruded to prism boundary layer and mostly isotropic tetrahedra in the volume. This approach was quickly rejected for bad quality elements near the airfoil/hub junction and tip gap, as well as element count in range of 4.5 million cells for sizing relevant for RANS analysis. This approach was quickly dropped.

A non-trivial topology with fully conforming periodic boundaries was introduced (fig 4.3). This topology fulfills all the prerequisites stated apart from possibility to mesh a structural tip gap. Such approach makes it impossible from topological standpoint to place a structural mesh in this area. A RANS sufficient mesh without tip gap area (blade was extended to the casing surface) was created. The cell count for this mesh is below 0.5 million cells with better skewness and orthogonal quality. This mesh was utilized for numerical setup and data acquisition testing as it was faster to converge.

Final topology was a standard h-grid topology for airfoil 4.4. Although it is impossible to create a conforming periodic interface with such mesh topology, a fully structural tip gap was implemented. Omitting the blade-hub juncture fillet simplified the mesh. Such topology eradicates the necessity of placing 5-way topology points.

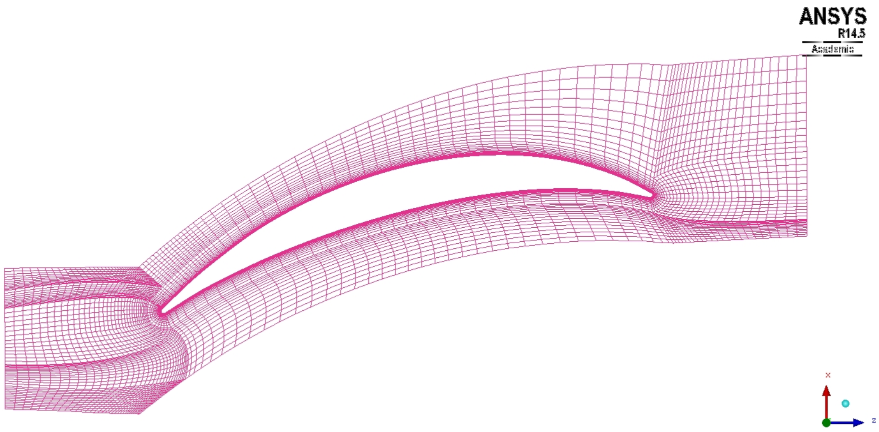

FIGURE 4.3: Mesh topology with conforming periodic boundaries

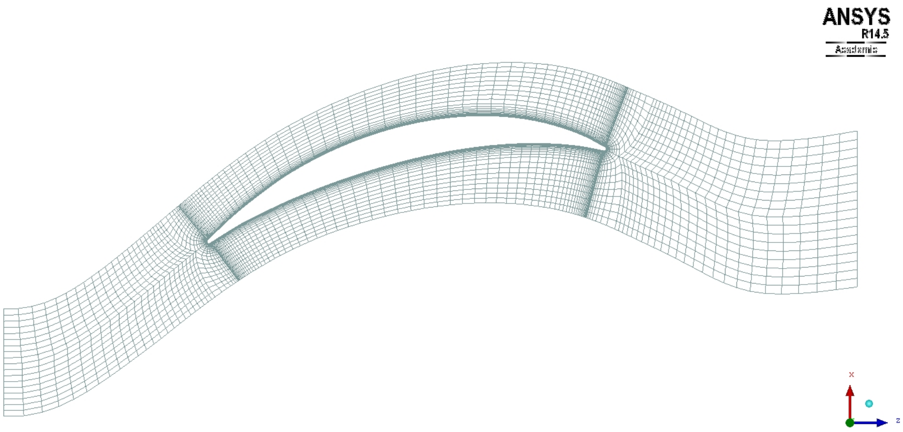

FIGURE 4.4: Mesh h-topology

Mesh was created in Ansys ICEM software using structural blocking method. The topology was sliced and associated to internal surfaces mentioned in the above section. This enforces mesh layering along design streamlines and provides high quality mesh on internal surfaces for flow field data acquisition further in the process. Blade wall boundary condition is distributed among five separate parts: blade pressure side, blade suction side, leading and trailing edges and tip surface.

Element sizing in volume and in tangent direction to the blade is limited to 3 mm, with 5 mm at inlet and outlet boundary conditions. The mesh sizing requirements are described in chapter 3. Blade boundary layer is produced by creating an o-grid around blade geometry. Hub and casing boundary layers are created by changing the sizing on the blocks adjacent to the geometry. Sizing of the first element is estimated with y+ parameter as described in equation: 4.3. First element thickness in on the blade surfaces ranges from is $2\mu m$ on tip airfoil and $10\mu m$ on hub airfoil. This corresponds to $y^+ \approx 2$ calculated by streamline velocity values given in [15].

$$\Delta s = \frac{y^+ \mu}{U_{fric} \rho} \tag{4.3}$$

Where:

$$U_{fric} = \sqrt{\frac{\tau_{wall}}{\rho}} \tag{4.4}$$

Where:

$$\tau_{wall} = \frac{C_f \rho U_\infty^2}{2} \tag{4.5}$$

Where:

$$C_f = \frac{0.026}{Re_x^{1/7}} \tag{4.6}$$

Figure 4.5, provides overview of mesh quality defined by figure 4.1. Created mesh is of high quality and is sufficient for both RANS (chapter 5) and DDES (chapter 6) analyses. Final mesh reached roughly 11.5 million cell count. Final mesh is presented in figure 4.6

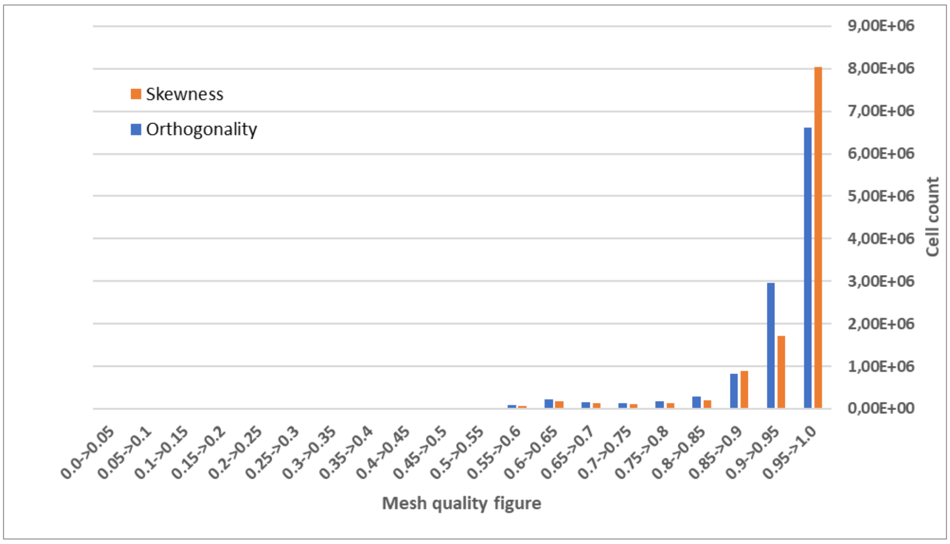

FIGURE 4.5: Mesh non-orthogonality histogram

4.4 Case preprocessing

CFD analyses for generating raw pressure field data are performed in ANSYS Fluent 17.2 software on Prometheus HPC cluster located in Kraków. Access for this infrastructure was granted by PLGrid infrastructure. Calculations were run on 5 nodes of 24CPU cores and 128GB RAM each [18], which resulted in decomposition to 120 cores, resulting in allocating around 110 thousand cells to a single HPC core.

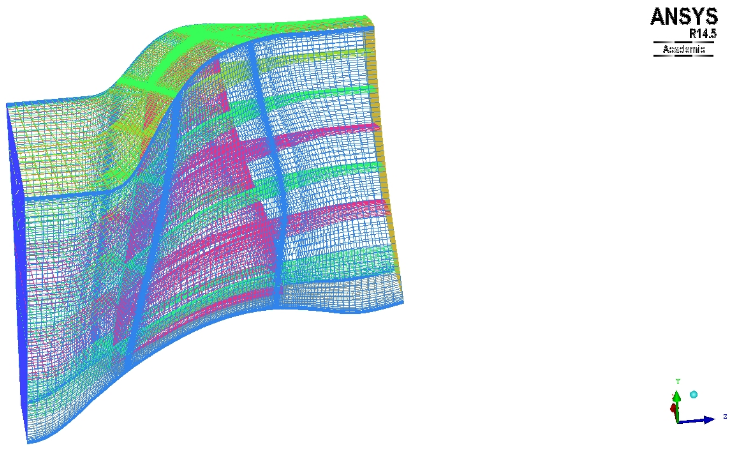

FIGURE 4.6: Completed Mesh

Following is the numerical setup for all of the performed analyses. The setup corresponds to "peak efficiency conditions" of the experimental compressor.

4.4.1 General settings and material properties

Analysis was resolved using implicit density based solver. The theory behind the solver is described in chapter 3. Material used in the anaysis resembles standard air modeled as ideal gas as in equation with following properties described in table 4.1

TABLE 4.1: Standard air properties

C_p	1006.43	$\frac{J}{kg \cdot K}$
λ	0.0242	$\frac{W}{m \cdot K}$
μ	1.7894e-05	$\frac{kg}{m \cdot s}$
M	28.966	$\frac{kg}{kmol}$

$$pV = nRT \tag{4.7}$$

Analysis operating pressure is set to 0 Pascal, which is a standard practice in compressible flow CFD.

Fluid zone is set as "frozen rotor" - rotating reference frame. Although no mesh motion is implied, the effect of Coriolis accelerations and centrifugal acceleration will be taken into account by adding respective acceleration components to momentum equations as described in chapter 3. The rotational velocity is set to 1680 rad/s.

4.4.2 Boundary conditions

Following boundary conditions were applied to the mesh boundaries. Following setup is again typical for compressible flow CFD.

Table 4.2: Test case boundary conditions

Boundary marker	Boundary type		
Inlet	Pressure Inlet	101350	Pa
Outlet	Pressure Outlet	102000	Pa
Hub	Movig wall	1680	rad/s
Blade	Moving wall	1680	rad/s
Casing	Stationary wall		
Internal profiles	Internal		
Periodic boundaries	Interface		

Moving wall boundaries represent the rotational velocity of the compressor blade and are necessary for stationary reference frame formulation. Boundary condition setup is no different to usual setups of analyses of such kind.

4.5 Data acquisition

Mesh and case is set up for possibly efficient data acquisition of flow field pressure and velocity data. FLUENT data file from a single timestep takes around 2GB of disk space. Saving such dataset from every of 50150 timesteps requires about 97TB of storage, which was unavailable at the time.

Data was gathered from blade surface (5 boundary markers) and 13 internal markers. Following node data values were saved:

- Static pressure
- Velocity magnitude (only internal markers)
- Vorticity magnitude (only internal markers)
- Static density
- Static temperature
- Node coordinates

This approach generated 18 datasets of 50510 files each, resulting in taking up 5.5TB of HPC cluster storage. The number of data is still large but manageable with current software engineering tools. Data was saved to ASCII text files.

Chapter 5

RANS Analysis

5.1 Main Section 1

Lorem ipsum dolor sit amet, consectetur adipiscing elit. Aliquam ultricies lacinia euismod. Nam tempus risus in dolor rhoncus in interdum enim tincidunt. Donec vel nunc neque. In condimentum ullamcorper quam non consequat. Fusce sagittis tempor feugiat. Fusce magna erat, molestie eu convallis ut, tempus sed arcu. Quisque molestie, ante a tincidunt ullamcorper, sapien enim dignissim lacus, in semper nibh erat lobortis purus. Integer dapibus ligula ac risus convallis pellentesque.

5.1.1 Subsection 1

Nunc posuere quam at lectus tristique eu ultrices augue venenatis. Vestibulum ante ipsum primis in faucibus orci luctus et ultrices posuere cubilia Curae; Aliquam erat volutpat. Vivamus sodales tortor eget quam adipiscing in vulputate ante ullamcorper. Sed eros ante, lacinia et sollicitudin et, aliquam sit amet augue. In hac habitasse platea dictumst.

5.1.2 Subsection 2

Morbi rutrum odio eget arcu adipiscing sodales. Aenean et purus a est pulvinar pellentesque. Cras in elit neque, quis varius elit. Phasellus fringilla, nibh eu tempus venenatis, dolor elit posuere quam, quis adipiscing urna leo nec orci. Sed nec nulla auctor odio aliquet consequat. Ut nec nulla in ante ullamcorper aliquam at sed dolor. Phasellus fermentum magna in augue gravida cursus. Cras sed pretium lorem. Pellentesque eget ornare odio. Proin accumsan, massa viverra cursus pharetra, ipsum nisi lobortis velit, a malesuada dolor lorem eu neque.

5.2 Main Section 2

Sed ullamcorper quam eu nisl interdum at interdum enim egestas. Aliquam placerat justo sed lectus lobortis ut porta nisl porttitor. Vestibulum mi dolor, lacinia molestie gravida at, tempus vitae ligula. Donec eget quam sapien, in viverra eros. Donec pellentesque justo a massa fringilla non vestibulum metus vestibulum. Vestibulum in orci quis felis tempor lacinia. Vivamus ornare ultrices facilisis. Ut hendrerit volutpat vulputate. Morbi condimentum venenatis augue, id porta ipsum vulputate in. Curabitur luctus tempus justo. Vestibulum risus lectus, adipiscing nec condimentum quis, condimentum nec nisl. Aliquam dictum sagittis velit sed iaculis. Morbi tristique augue sit amet nulla pulvinar id facilisis ligula mollis. Nam elit libero, tincidunt ut aliquam at, molestie in quam. Aenean rhoncus vehicula hendrerit.

Chapter 6

DDES Analysis

6.1 Main Section 1

Lorem ipsum dolor sit amet, consectetur adipiscing elit. Aliquam ultricies lacinia euismod. Nam tempus risus in dolor rhoncus in interdum enim tincidunt. Donec vel nunc neque. In condimentum ullamcorper quam non consequat. Fusce sagittis tempor feugiat. Fusce magna erat, molestie eu convallis ut, tempus sed arcu. Quisque molestie, ante a tincidunt ullamcorper, sapien enim dignissim lacus, in semper nibh erat lobortis purus. Integer dapibus ligula ac risus convallis pellentesque.

6.1.1 Subsection 1

Nunc posuere quam at lectus tristique eu ultrices augue venenatis. Vestibulum ante ipsum primis in faucibus orci luctus et ultrices posuere cubilia Curae; Aliquam erat volutpat. Vivamus sodales tortor eget quam adipiscing in vulputate ante ullamcorper. Sed eros ante, lacinia et sollicitudin et, aliquam sit amet augue. In hac habitasse platea dictumst.

6.1.2 Subsection 2

Morbi rutrum odio eget arcu adipiscing sodales. Aenean et purus a est pulvinar pellentesque. Cras in elit neque, quis varius elit. Phasellus fringilla, nibh eu tempus venenatis, dolor elit posuere quam, quis adipiscing urna leo nec orci. Sed nec nulla auctor odio aliquet consequat. Ut nec nulla in ante ullamcorper aliquam at sed dolor. Phasellus fermentum magna in augue gravida cursus. Cras sed pretium lorem. Pellentesque eget ornare odio. Proin accumsan, massa viverra cursus pharetra, ipsum nisi lobortis velit, a malesuada dolor lorem eu neque.

6.2 Main Section 2

Sed ullamcorper quam eu nisl interdum at interdum enim egestas. Aliquam placerat justo sed lectus lobortis ut porta nisl porttitor. Vestibulum mi dolor, lacinia molestie gravida at, tempus vitae ligula. Donec eget quam sapien, in viverra eros. Donec pellentesque justo a massa fringilla non vestibulum metus vestibulum. Vestibulum in orci quis felis tempor lacinia. Vivamus ornare ultrices facilisis. Ut hendrerit volutpat vulputate. Morbi condimentum venenatis augue, id porta ipsum vulputate in. Curabitur luctus tempus justo. Vestibulum risus lectus, adipiscing nec condimentum quis, condimentum nec nisl. Aliquam dictum sagittis velit sed iaculis. Morbi tristique augue sit amet nulla pulvinar id facilisis ligula mollis. Nam elit libero, tincidunt ut aliquam at, molestie in quam. Aenean rhoncus vehicula hendrerit.

Chapter 7

Results of flow field noise analysis

7.1 Transition from flow-field to sound signal data

The performed DDES analysis delivered a set of files for further postprocessing. Values of static pressure, velocity magnitude, vorticity magnitude, static density and static temperature were gathered from designated boundaries and internal surfaces representing the design streamline cones. The dataset consists of 50150 files for each of the 13 internal surfaces and 5 blade boundaries, resulting in over 5.5 TB of data.

This set was postprocessed to obtain the sound pressure, sound intensity and their respective decibel values for each time step. The mathematical formulas for obtaining these values are provided in chapter /refapproach and the `Python 3.5x` implementation of which is presented in appendix A. The postprocessing of flow field data to sound data was performed on the same HPC infrastructure as the DDES analysis, due to the file accessibility. Postprocessed dataset was saved in a folder structure resembling the source files. The dataset consists of 902 700 files and another 5.5TB of data in form of comma separated values.

7.2 RMS results

The sound values were then further processed to obtain the Root Mean Square values of sound pressure and sound intensity from internal markers and blade surfaces. Scatter/-contour plots of the given values are provided the figures **??** thru **??** below. Providing data for both pressure and intensity values and their decibel levels is redundant, yet shown for clarity and direct comparison of given values.

Internal boundary plots provide information on maximum and minimum values of SPL and SPLdB presented on the plot. As the minimum sound intensity (SIL) is equal 0 and the SILdB values for corresponding points approach negative infinity. Such values were overridden to show 0 SILdB on the plot. For this reason minimum value coordinates are omitted in the plot description

Blade surface plot is composed by plotting five datasets on one canvas and manipulating the sign of the canvas x-axis to mimic various view projections. Tool used to generate the scatter plots for blade surface overlaps the datapoints that share the same canvas x and canvas y coordinates, therefore the plotting order is always "back-to-front", so that the surface closest to the viewer is plotted atop the canvas.

Sound pressure and intensity plots are scaled with a normalised logarithmic colorbar with common scale across all of the internal surface and blade surface plots. For sound pressure, the maximum obtained value is $13917.395[Pa]$, so the maximum value of the colorbar is liberally rounded up to $15000[Pa]$. Minimum value for SPL is in range of $10[Pa]$, so the lower bar limit is set to zero. As for the Decibel values the lowest obtained value is around $116dB$, largest - around $177dB$. The colorbar scale is therefore set to 100 - 180 dB range with linear scale. The same approach was used for maximum values of sound intensity. For sound intensity itself, the colorbar was limited from $0W/m^2$ to $1.2 \cdot 10^6[W/m^2]$ and normalized to logarithmic scale. For SILdB plot, the bar range is limited to $0dB$ to $180dB$ range with linear scale. More details on RMS values are presented in section 7.3.

Plots are created by projecting points from 3D surface onto a 2D plane of the plot, therefore some shape aberrations may occur. Color of the point is normalized as described above. The axes names correspond to the global coordinate system axes.

PLOTS GO HERE

7.3 Initial conclusions

The qualitative analysis of the internal surfaces shows, that the main source of pressure fluctuations is the turbulence resulting from the separation of flow. Such separations can be induced by the typical airfoil flow phenomena of backflow in the boundary layer, or by shockwave–boundary layer interactions.

Chapter 8

Conclusions & Further work

8.1 Main Section 1

Lorem ipsum dolor sit amet, consectetur adipiscing elit. Aliquam ultricies lacinia euismod. Nam tempus risus in dolor rhoncus in interdum enim tincidunt. Donec vel nunc neque. In condimentum ullamcorper quam non consequat. Fusce sagittis tempor feugiat. Fusce magna erat, molestie eu convallis ut, tempus sed arcu. Quisque molestie, ante a tincidunt ullamcorper, sapien enim dignissim lacus, in semper nibh erat lobortis purus. Integer dapibus ligula ac risus convallis pellentesque.

Nunc posuere quam at lectus tristique eu ultrices augue venenatis. Vestibulum ante ipsum primis in faucibus orci luctus et ultrices posuere cubilia Curae; Aliquam erat volutpat. Vivamus sodales tortor eget quam adipiscing in vulputate ante ullamcorper. Sed eros ante, lacinia et sollicitudin et, aliquam sit amet augue. In hac habitasse platea dictumst.

8.1.1 Subsection 2

Morbi rutrum odio eget arcu adipiscing sodales. Aenean et purus a est pulvinar pellentesque. Cras in elit neque, quis varius elit. Phasellus fringilla, nibh eu tempus venenatis, dolor elit posuere quam, quis adipiscing urna leo nec orci. Sed nec nulla auctor odio aliquet consequat. Ut nec nulla in ante ullamcorper aliquam at sed dolor. Phasellus fermentum magna in augue gravida cursus. Cras sed pretium lorem. Pellentesque eget ornare odio. Proin accumsan, massa viverra cursus pharetra, ipsum nisi lobortis velit, a malesuada dolor lorem eu neque.

8.2 Main Section 2

Sed ullamcorper quam eu nisl interdum at interdum enim egestas. Aliquam placerat justo sed lectus lobortis ut porta nisl porttitor. Vestibulum mi dolor, lacinia molestie gravida at, tempus vitae ligula. Donec eget quam sapien, in viverra eros. Donec pellentesque justo a massa fringilla non vestibulum metus vestibulum. Vestibulum in orci quis felis tempor lacinia. Vivamus ornare ultrices facilisis. Ut hendrerit volutpat vulputate. Morbi condimentum venenatis augue, id porta ipsum vulputate in. Curabitur luctus tempus justo. Vestibulum risus lectus, adipiscing nec condimentum quis, condimentum nec nisl. Aliquam dictum sagittis velit sed iaculis. Morbi tristique augue sit amet nulla pulvinar id facilisis ligula mollis. Nam elit libero, tincidunt ut aliquam at, molestie in quam. Aenean rhoncus vehicula hendrerit.

Appendix A

Code for direct formulation of noise analysis

```
# dask-noise.py
print("Loading Libraries...")
import os, sys
import csv
import platform
import numpy as np
import pandas as pd
import dask.dataframe as dd
import math
print("Loaded Libraries...")
print("Starting code...")
print("Loading directories..")
path_data = './flow-data/<folder_name>'
path_acu = './noise-data/<folder_name>/acu'
print("Loaded directories...")
print("Loading batch data...")
os.chdir(path_data)
batch_data = dd.read_csv('*.dat', delimiter=r"\s+", decimal='.')
print("Batch data done...")
print("Calculating batch averages...")
averages = pd.DataFrame(batch_data.groupby('nodenumber').mean().compute())
print("Batch averages done...")
print("Generating average pressure dataframe")
avg_static_p = pd.DataFrame({'pressure': averages['pressure']})
print("Generating average velocity dataframe")
avg_rel_v = pd.DataFrame(
                {'rel-velocity-magnitude': averages['rel-velocity-magnitude']})
print("Generating node coordinates...")
node_coords = pd.DataFrame({
    'x-coordinate': averages['x-coordinate'],
    'y-coordinate': averages['y-coordinate'],
    'z-coordinate': averages['z-coordinate']
})
del(batch_data)
print("Batch data deleted...")
```

```
print("Listing files...")
filelist = sorted(os.listdir(path_data))[len(os.listdir(path_acu)):]
print("Starting noise analysis loop...")
for file in filelist:
    os.chdir(path_data)
    timestep = str(os.path.basename(str(file)))[7:-4]
    time_static_p = pd.DataFrame(pd.read_csv(file, delimiter=r"\s+"))
        .set_index('nodenumber')
    acoustic_p = time_static_p.subtract(avg_static_p, fill_value=None)
    spl_db = acoustic_p.apply(lambda x: 20 * np.log10(np.abs(x)/0.00002), axis=1)
    time_rel_vel = pd.DataFrame(pd.read_csv(file, delimiter=r"\s+"))
        .set_index('nodenumber')
    particle_v = time_rel_vel.subtract(avg_rel_v, fill_value=None).abs()
    sound_intensity = pd.DataFrame(
        acoustic_p.values*particle_v.values,
        index=acoustic_p.index)
    sil_db = sound_intensity.apply(
        lambda x: 10 * np.log10(np.abs(x)/1e-12), axis=1)
    acoustic_data = pd.concat(
        [node_coords,
        acoustic_p,
        spl_db,
        particle_v,
        sound_intensity,
        sil_db], axis=1)
    acoustic_data.columns =
        ['x-coordinate',
        'y-coordinate',
        'z-coordinate',
        'sound-pressure',
        'spl-db',
        'particle-velocity',
        'sound-intensity',
        'sil-db']
    os.chdir(path_acu)
    acoustic_data.to_csv(str('<filename>_' + str(timestep) + '.dat'), sep=',')
    print(str('<filename>' + str(timestep) + '.dat done...'))
print("Exiting noise analysis loop...")
print("Script done, exiting.")
```

Appendix B

Code for discrete Fourier analysis

```
#fft.py
print("Loading Libraries...")
import os
import csv
import platform
import numpy as np
from scipy.fftpack import fft
import pandas as pd
import dask.dataframe as dd
import math
print("Loaded Libraries...")
print("Starting code...")
print("Loading directories..")
path_acu = './noise-data/<folder_name>/acu'
path_fft = './results/fft'
print("Loaded directories...")
print("Loading batch data...")
os.chdir(path_acu)
batch_pressure = dd.read_csv('*.dat',
                                delimiter=",",
                                decimal='.',
                                usecols=["nodenumber", "sound-pressure"])
batch_pressure = batch_pressure.set_index("nodenumber")
print("Batch data done...")
print("Calculating FFT...")
batch_fft = batch_pressure.groupby('nodenumber').apply(
                                lambda x: fft(x),
                                meta=('node-fourier-series', 'f8')
                                ).compute()
print("FFT Done..")
print("Saving FFT to dataframe...")
#node_fft_max.set_index('nodenumber')
os.chdir(path_fft)
batch_fft.to_csv(str('<file_name_fft>.dat'), sep=",")
print("Dataframe saved...")
print("Script completed...")
```

Appendix C

Code for RMS computation

```
#rms.py
print("Loading Libraries...")
import os
import csv
import platform
import numpy as np
from scipy.fftpack import fft
import pandas as pd
import dask.dataframe as dd
import math
import matplotlib.pyplot as plt
print("Loaded Libraries...")

#PLGRID
print("Loading directories..")
path_acu = './noise-data/<folder_name>/acu'
path_rms = './results/rms'
print("Loaded directories...")

print("Loading batch data...")
os.chdir(path_acu)
batch_data = dd.read_csv('*1.dat',
                        delimiter=",",
                        decimal='.',
                        usecols=["nodenumber", "sound-pressure", "sound-intensity"])
batch_data = batch_data.set_index("nodenumber")
print("Batch data done...")

print("Calculating rms...")
rms = pd.DataFrame(batch_data.groupby('nodenumber').std().compute())
rms['rms_spldb'] = rms['sound-pressure'].apply(lambda x: 20*np.log10(x/0.00002))
rms['rms_sildb'] = rms['sound-intensity'].apply(lambda x: 10*np.log10(x/1e-12))

print("Saving...")
os.chdir(path_rms)
rms.to_csv(str('<filename>'), sep=",")
```

Appendix D

Blade design surface coordinates

Write your Appendix content here. [1] [2] [3] [4] [16] [13] [14] [15]

Bibliography

[1] M. J. Lighthill. On sound generated aerodynamically i. general theory. *Proceedings of the Royal Society. Series A, Mathematical, Physical and Engineering Sciences*, 211 (1107):564–587, March 1952. URL http://rspa.royalsocietypublishing.org/content/211/1107/564.

[2] M. J. Lighthill. On sound generated aerodynamically ii. turbulence as a source of sound. *Proceedings of the Royal Society. Series A, Mathematical, Physical and Engineering Sciences*, 222(1148):1–32, March 1954. URL http://rspa.royalsocietypublishing.org/content/222/1148/1.

[3] N. Curle. The influence of solid boundaries upon aerodynamic sound. *Proceedings of the Royal Society. Series A, Mathematical, Physical and Engineering Sciences*, 231(1187):505–514, September 1955. URL http://rspa.royalsocietypublishing.org/content/231/1187/505.

[4] D. L. Hawkings J. E. Ffowcs Williams. Sound generation by turbulence and surfaces in arbitrary motion. *Philosophical Transactions of the Royal Society of London. Series A, Mathematical and Physical Sciences*, 264(1151):321–342, May 1969. URL http://www.jstor.org/stable/73790.

[5] Ansys documentation. fluent theoru guide. *SAS IP Inc.*, Release 17.2, 2015.

[6] K. S. Brentner and F. Farassat. An analytical comparison of the acoustic analogy and kirchhoff formulations for moving surfaces. *AIAA Journal*, 36(8):1379–1386, 1998.

[7] P. Moin C. Choi. Grid-point requirements for large eddy simulation: Chapman's estimates revisited. *Physics of Fluids*, 24(1), January 2012. URL https://aip.scitation.org/doi/full/10.1063/1.3676783.

[8] J. Smagorinsky. General circulation experiments with the primitive equations. *Monthly Weather Review*, 91(3), 1963.

[9] P. Sagaut C. Wagner, T. Hüttl. Large-eddy simulation for acoustics. *Cambridge University Press*, 2007.

[10] J. O. Hinze. Turbulence. *McGraw-Hill Publishing Co.*, 1975.

[11] M. Strelets P. R. Spalart, W. H. Jou and S. R. Allmaras. Comments of feasibility of les for wings, and on a hybrid rans/les approach. *First International conference: Advances in DNS LES: Direct numerical simulation and large eddy simulation*, pages 137–148, 1997.

[12] et. al. P. R. Spalart. A new version of detached-eddy simulation, resistant to ambiguous grid densities. *Theoretical and Computational Fluid Dynamics*, 20:181–195, 2006.

[13] W. Stevans W. S. Cunnan and D. C. Urasek. Design and performance of a 427-meter-per-second-tip-speed two stage fan having a 2.40 pressure ratio. *NASA Technical Paper*, (TP-1314), October 1978.

[14] W. T. Gorrel D. C. Urasek and W. S. Cunnan. Performance of a two-stage fan having a low-aspect-ratio, first-stage rotor blading. *NASA Technical Paper*, (TP-1493), August 1979.

[15] M. D. Hathaway A. J. Strazisar, J. R. Wood and Kenneth L. Suder. Laser anemometer measurements in a transonic axial-flow fan rotor. *NASA Technical Paper*, (TP-2897), November 1989.

[16] J. S. David C. Janetzke J. E. Crouse and R. E. Schwirian. A computer program for composing blading from simulated circular-arc elements on conical surfaces. *NASA Technical Note*, (TN D-5437), September 1969.

[17] J. Mosiezny. Github repository for nasa r67 input data and noise analysis. 2018. URL `https://github.com/JedrzejMosiezny/R67-data-analysis`.

[18] Prometheus computation resources. 2018. URL `https://kdm.cyfronet.pl/portal/Prometheus`.